On the Structure of an Asymmetric Carbon Membrane with a Novolac Resin Precursor

TH. STERIOTIS,[1] K. BELTSIOS,[1] A. CH. MITROPOULOS,[1] N. KANELLOPOULOS,[1] S. TENNISON,[2] A. WIEDENMAN,[3] U. KEIDERLING[3]

[1] NCSR Demokritos, Institute of Physical Chemistry, 153 10 Ag. Paraskevi Attikis, Greece

[2] BP International Limited, Sunbury-on-Thames, Middlesex TW 16 7LN, United Kingdom

[3] Hahn Meitner Institut, BENSC, Glienicker Strasse s 100, D-1000 Berlin, Germany

Received 15 March 1996; accepted 20 November 1996

ABSTRACT: An asymmetric tubular carbon membrane, appropriate for gas separation applications, was made through carbonization at 800°C of a precursor structure containing two phenol-formaldehyde resins, a partially cured novolac resin in 30–60 μm grains (bulk material), and a resole resin (membrane skin material). A replica of the skin material was deposited separately on a stainless steel substrate. The samples were analyzed by nitrogen adsorption, small-angle neutron scattering, and scanning electron microscopy (SEM). The basic structural entities of both skin and the bulk part were low-aspect-ratio carbon domains with a characteristic dimension in the 4.0–4.5 nm range. Further, the materials were characterized by microporosity in the 0.30–0.50 range with isotropic pores having a 1.3 nm diameter. The results are discussed with the help of a systematic survey of possible carbon structures with an intermediate level of microporosity. © 1997 John Wiley & Sons, Inc. J Appl Polym Sci **64:** 2323–2345, 1997

Key words: novolac resin; carbon membranes; carbon microstructure; micropores; nitrogen adsorption; small-angle neutron scattering (SANS)

1. INTRODUCTION

The carbonization of polymeric materials in fiber, membrane, and bulk form leads to structures approaching the hexagonal structure of graphite, characterized by a 3.354 Å interlayer spacing. Depending on the polymeric precursor (carbon and cross-link content and other structural details) and the carbonization conditions (times, temperatures, atmosphere, and presence of stress), the product may approach the graphitic structure to various degrees (with regard to crystallinity, interlayer spacing, and domain size). In addition, the final product may have a (nearly) compact form or develop considerable porosity at one or more levels (i.e., microporosity with a pore width below 2 nm, mesoporosity with pores in the 2–50 nm range, and macroporosity for larger pores; see, for example, Gregg and Sing[1,2]).

The maximum temperature of processing is a major factor affecting the size and interplanar spacing of the evolving carbon domains, though other factors, including the presence of stress/tension (especially in cases such as the carbonization of fibers under uniaxial tension), can also have a pronounced effect.[3,4] Typically, the evolving carbon domains have characteristic dimensions in the 3–10 nm range when processed at a maximum

Correspondence to: K. Beltsios.

Contract grant sponsors: Joule and Brite-Euram.
Contract numbers: JOF3-CT 95-0008 (Joule) and Breu-CT92-0568 (Brite-Euram).

temperature in the range of 1000°C (low-temperature carbonization). Further processing at temperatures often above 2100 or even 2800°C,[5–8] are necessary for the formation of domains having a linear dimension larger by an order of magnitude and an improved intradomain organization as well.

Regarding the final processing step, those structures with some interdomain organization (as a result of the preservation, induction, or enhancement of order during low-temperature carbonization) require relatively mild final processing conditions (e.g., a maximum processing temperature of 2100°C) for the formation of large ordered domains. On the other hand, materials with strongly disordered structures (such as those with heavily cross-linked precursors or poorly preserved original order) require quite intense final processing for the formation of large ordered domains; actually, they may instead develop strongly interwoven graphitic sheaths (glassy carbon), especially when the processed object has a pronounced three-dimensional form. Regarding porosity, this is a structural feature affected by a rather broad variety of processing parameters, and no general statements focusing on a single parameter (such as the maximum processing temperature) can be made about its type (pore size and shape) and extent.

In recent years, small-angle neutron scattering (SANS) has become a valuable tool for the characterization of porous materials, especially in combination with an independent experimental technique, such as adsorption of vapors (see, for example, Mitropoulos et al.[9]). The material of the present study is an asymmetric tubular carbon membrane based on two phenol-formaldehyde resin precursors processed to a maximum temperature of 800°C. Carbonaceous materials of this and a similar type are appropriate for a wide range of separation processes (see, for example, Simitzis et al.[10]). Our product finds a use as a gas separation (G-S) membrane; and a SANS, nitrogen adsorption, and scanning electron microscopy (SEM) study was undertaken for the purpose of understanding and eventually optimizing its structural features.

In an asymmetric membrane, the structure of the skin may exhibit some significant differences from that of the bulk material, at one or more length scales. However, the skin cannot be detached easily from the rest of the membrane, while its contribution to the SANS spectrum and adsorption isotherm profile of the composite structure is, in general, masked by the contribution from the bulk material. To circumvent this problem, we studied both the original membrane and a removable replica of the original skin deposited on a stainless steel plate (see the Experimental Section).

Structural descriptions for the skin and the bulk of the membrane, compatible with the obtained experimental information, will be presented in this article, which is organized as follows. Sections 3.1.a and 3.1.b of the Results and Discussion part refer to the global structure of the asymmetric membrane, while the rest is concerned primarily with the local structure (size scale $< 10^1$ nm). The local structure is the most important for G-S applications and also the most difficult to assess. In Section 3.2.a, we discuss a simple working model of local structure, based on the packing of single-sized spherical carbon domains. An analysis of porosity, surface area, and solid domain size data is presented in sections 3.2.b and 3.2.c. Refined models for the local structure compatible with the experimentally obtained information (porosity level, asymmetry and size range of pores, surface area range, and size range of solid domains) are found and analyzed in sections 3.2.d and 3.2.e, with the help of a general survey of carbon microstructures exhibiting an intermediate level of microporosity (0.35–0.55). That approach allowed for the evaluation of a significant range of candidate structures and thus reduced the arbitrariness in the choice of structural models. Three strong candidate structures are found, and a preference for one of them is indicated with the help of a dimensionality argument. Likely mechanisms for the generation of the proposed structural features are outlined in Section 3.2.f.

2. EXPERIMENTAL

2.1. Material Preparation

The bulk part of the precursor material was based on a dough containing 30–60 μm granules of a commercial phenol-formaldehyde novolac resin partially cross-linked at 130°C with a few percent of hexamethylene-tetramine. In addition to the resin granules, the dough contains water and commercial polymeric binders.

The top layer (skin) of the tubular membrane

was made through spraying, on the extruded cylindrical bulk precursor material, of an ethanol solution of a phenol-formaldehyde resole resin. The thickness of the top layer is in the 15–50 μm range, the tube diameter of the end product is approximately 0.7 cm, and its length is 30 cm.

The replica of the top layer was made through spraying on a stainless steel plate of the material used for the original top layer. The replica was then removed from the plate in the form of small chunks.

Both the tubular membrane and the replica of the skin layer were carbonized at a constant heating rate (50°C/h) in a nitrogen atmosphere to a maximum temperature of 800°C. Subsequently, the membrane could be activated at 800°C under carbon dioxide flow. For the study of the process of activation, we used a series of powder replicas of the skin material carbonized to a maximum of 800°C and subsequently activated for various times (samples Nos. 1–5).

2.2. SANS Measurements

Small-angle neutron scattering experiments have been conducted at the Hahn-Meitner-Institut (HMI), Berlin. The incoming neutrons were monochromized by a mechanical speed selector and collimated on a variable length from 1 to 16 m. A two-dimensional ^{3}He detector with 32 × 32 elements of 10 × 10 mm was used.[11] Data were collected for the (0.04 nmÅ^{-1}, 3.5 nm^{-1}) range of Q values, where Q is the scattering vector, and subsequently corrected for detector efficiency, absolute intensity calibration, and background. Membrane samples will, in general, contain a small contribution from the skin, most probably nondetectable by SANS, and, consequently, may be considered as bulk samples. As a result, for skin structure information, one has to rely on measurements performed on the unactivated skin replica material.

In the small-angle scattering (SAS) practice, either with neutrons or X-rays, most of the structural information is contained in the following interval:

$$0 \leq Q \cdot d \leq 2\pi \qquad (1.1)$$

where d is a characteristic dimension of the structure, and $Q = \dfrac{4\pi \sin \theta}{\lambda}$, where 2θ is the scattering angle, and λ is the wavelength. For an isotropic medium, the spherically scattered intensity may be written as[12]

$$I(Q) = 4\pi\rho^2 V \int \gamma(r) r^2 \frac{\sin (Q \cdot r)}{Q \cdot r}\, dr \qquad (1.2)$$

where ρ is the scattering length density, V is the scattering volume, and $\gamma(r)$ is the correlation function at point r. The above equation reduces to two well-known simpler forms, in the two following special cases.

1) When the inequality $Q \cdot d_{\min} \geq \pi$ holds, with $d_{\min}$ being the smallest characteristic dimension affecting scattering, eq. (1.2) reduces to Porod's Law,[12] as follows:

$$I(Q) = \frac{2\pi\rho^2 A}{Q^4} \qquad (1.3)$$

where A is the total surface area.

2) When the inequality $Q \cdot d_{\max} \leq \pi/6$ holds, we obtain the Guinier approximation,[12,13] as follows:

$$I(Q) = I_0 \exp\left(-\frac{Q^2 R_G^2}{3}\right) \qquad (1.4)$$

where I_0 is a constant, and R_G is the radius of gyration. Equations (1.3) and (1.4) are very useful in the analysis of SAS data.

2.3. Nitrogen Adsorption Measurements

The adsorption isotherms of nitrogen were measured volumetrically at 77 K. Experiments were carried out in an Autosorb-1 Quantachrome porosimeter. The materials measured were a ground bulk sample and unactivated and activated skin replica powder samples. The latter differ in form from the skin replica cast on a steel plate (original powders versus large chunks). All samples were outgassed at 10^{-7} mbar, and the isothermal profiles were recorded following the adsorption–desorption path. Pore size distribution, specific surface areas, and micropore volumes were calculated.

The nitrogen adsorption isotherms (Fig. 1) for all samples are of type-I, according to the Brunauer–Deming–Deming–Teller (BDDT) classi-

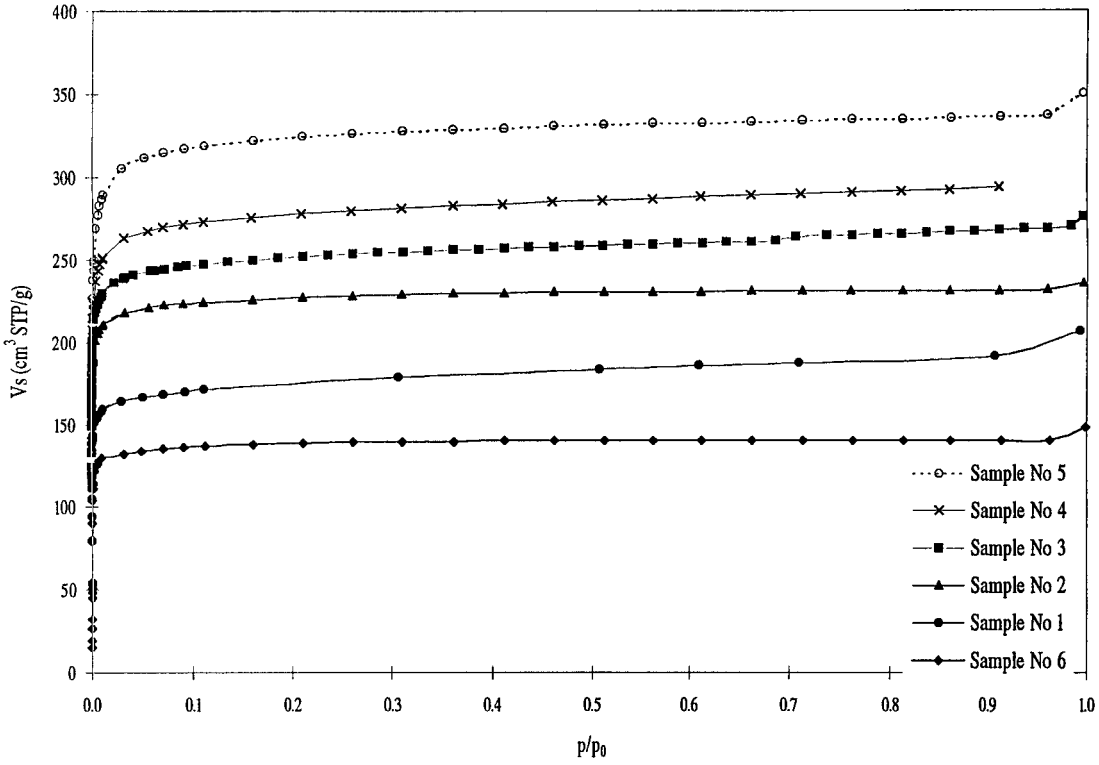

Figure 1 Nitrogen adsorption isotherms for activated and unactivated membrane materials. All isotherms are of Type I. For sample information, see Table I and Section 3.2.b.

fication,[14] which implies that the materials possess microporosity (i.e., pores with a diameter below 2 nm); and there are no obvious contributions from mesoporosity. The upward turn of the isotherm found for some of the samples near saturation ($p/p_o \rightarrow 1$) may reflect the presence of some intraparticle macroporosity (as in the case of the bulk sample and also for sample No. 5; see Section 3.2.b), but it may originate as well from the macropore-size interparticle spacing of the powders. Pore size distributions for bulk and activated and unactivated skin replica samples, calculated through the method of Dubinin and Astakhov (DA),[15] show, in all cases except for sample No. 5, a similar distribution with a maximum in pore radius at 0.65 nm [Fig. 2(a)]. For sample No. 5, the maximum shifts to a 0.75 nm radius value. The cited values pertain to the volume distribution. The number distribution [Fig. 2(b)] has its peaks at radii values smaller by approximately 0.05 to 0.02 nm. In addition, the number distribution for sample No. 4 deviates slightly from the corresponding distributions for samples No. 1–3.

Specific areas, total micropore volume (expressed per gram of material), and microporosities calculated from nitrogen porosimetry appear on Table I. It should be noted that the microporosity features cannot be currently assessed beyond any doubt.[16] A detailed description of the models used may be found, for example, in Lowell and Shields.[17] The DR (Dubinin–Radushkevich[18]) method assumes micropore filling and provides

Figure 2 (A) Volume distribution of pore radii via the DA method. For sample nos. 1–4 (unactivated and activated with a weight loss of 6.5, 10, and 16%, respectively) and sample no. 6 (bulk), the maximum of the distribution is at 0.65 nm. For the excessively activated Sample No. 5, the peak has shifted to 0.75 nm. (B) Number distribution of pore radii (assuming spherical shape) via the DA method. The maximum of the distribution occurs at 0.60 nm for sample Nos. 1–3 and no. 6, at 0.62 nm for Sample No. 4, and 0.70 nm for Sample No. 5.

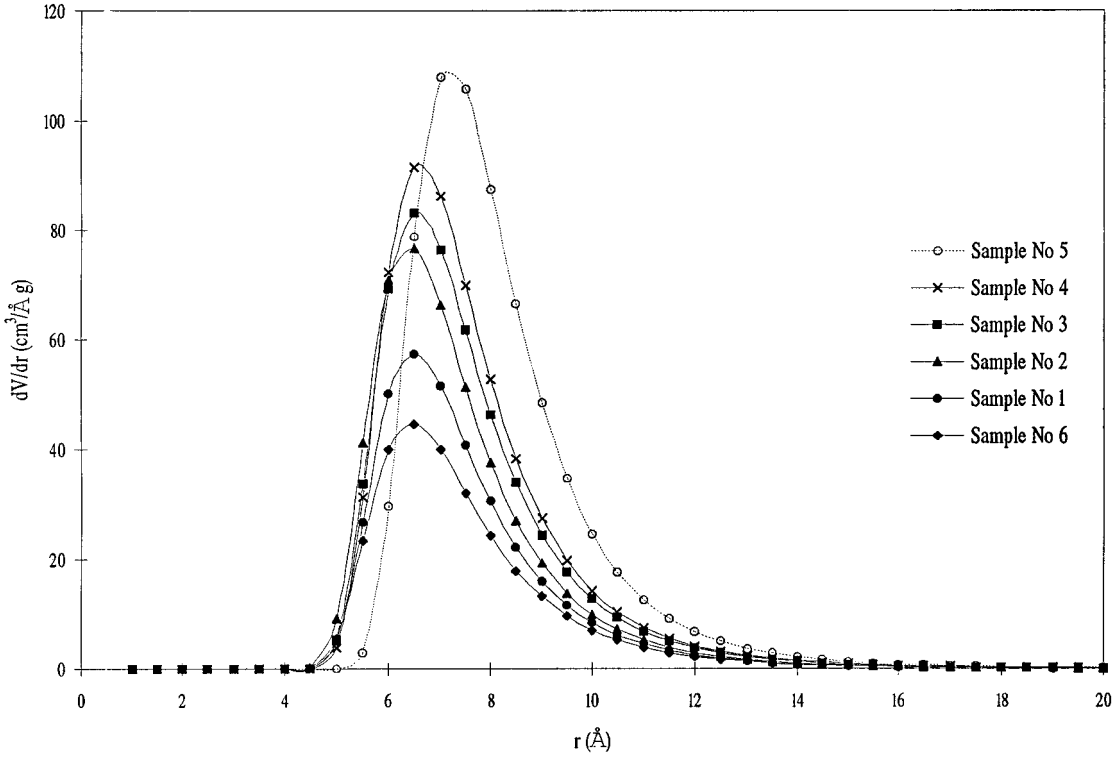
dV/dr (cm³/Å g)
r (Å)
Sample No 5
Sample No 4
Sample No 3
Sample No 2
Sample No 1
Sample No 6

(a)

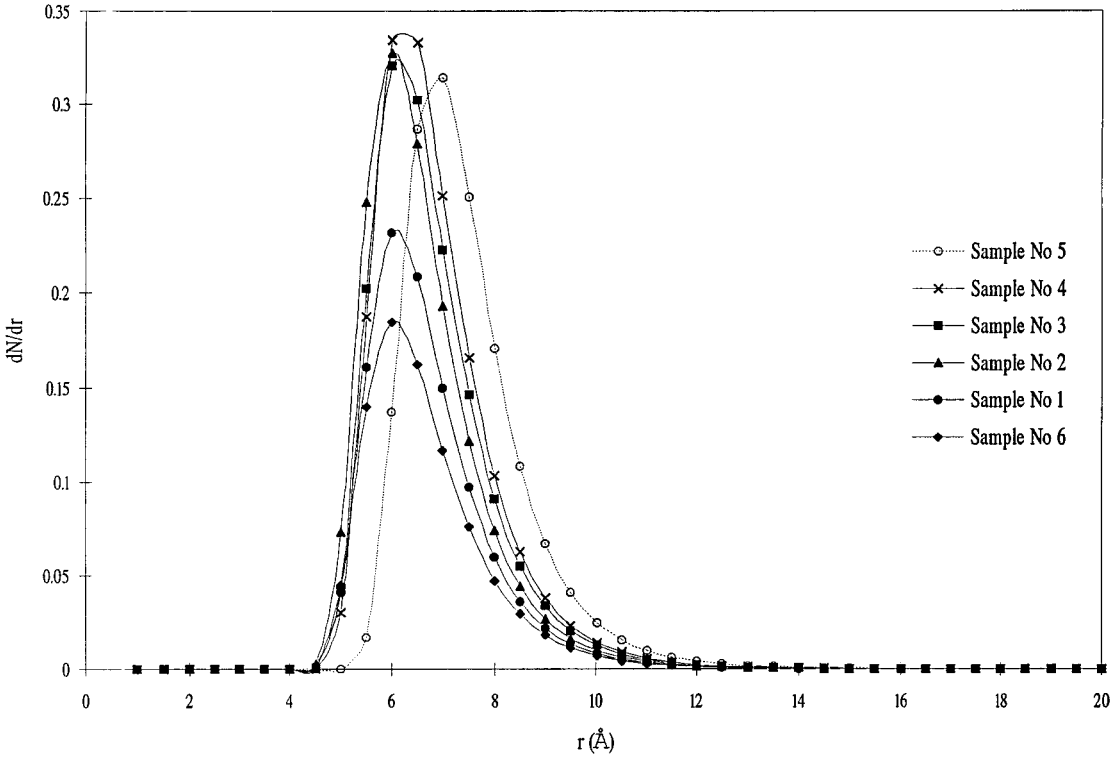
dN/dr
r (Å)
Sample No 5
Sample No 4
Sample No 3
Sample No 2
Sample No 1
Sample No 6

(b)

Table I N_2 Adsorption[19] and He-density Data for Various Samples

Sample	He-measured Density (g/cm^3)	Micropore Volume (cm^3/g)		Total (Micro)pore Volume (cm^3/g)	Surface Area (Mi) (m^2/g) (ca)			Calculated (Micro)porosity		
		Langmuir (V_L)	DR (V_{DR})	at $p/p_0 = 0.95$ ($V_{0.95}$)	BET	Langmuir	DRK	V_L	V_{DR}	$V_{0.95}$
No. 1	2.02	0.291	0.268	0.297	691	820	753	0.370	0.351	0.375
No. 2	2.04	0.359	0.351	0.360	913	1010	987	0.423	0.417	0.423
No. 3	2.11	0.405	0.390	0.420	1015	1139	1096	0.460	0.451	0.469
No. 4	2.06	0.451	0.426	0.456	1088	1269	1198	0.481	0.468	0.485
No. 5	2.2	0.521	0.507	0.523	1284	1465	1425	0.534	0.527	0.534
No. 6	2.02	0.217	0.217	0.217	562	610	611	0.305	0.305	0.305

Sample No. 1, unactivated skin replica sample; sample No. 2, activated No. 1 showing 6.5% weight loss; sample No. 3, activated No. 1 showing 10% weight loss; sample No. 4, activated No. 1 showing 16% weight loss; sample No. 5, activated No. 1 showing 30% weight loss; sample No. 6, unactivated bulk sample.

reliable estimates for microporosity. The DR extension by Kaganer (DRK[14,17]) uses a DR type of equation but assumes monolayer coverage and provides an estimate for the surface area. The Langmuir method assumes monolayer coverage, leading to the so-called monolayer capacity, which is also used for the calculation of a micropore volume. As the shape of isotherms does not indicate the presence of mesoporosity, the curves are used directly for the estimation of micropore volume ($V_{0.95}$) on the basis of experimental points for relative pressures from 0.90 to 0.95 (pore radii $<$ 10–11 nm). BET estimates are included for indicative purposes only, as the BET method is not considered reliable for microporous materials. For samples containing macroporosity (e.g., the bulk sample No. 6, the estimated microporosities correspond, as a volume fraction, to regions containing no macropores. Helium-measured densities provide the density of the compact material (material not penetrated by He gas).

3. RESULTS AND DISCUSSION

3.1. Global Membrane Structure

3.1.a. The Membrane Bulk

SEM photographs (Fig. 3) show that the bulk of the membrane possesses a structure containing openings in the range of 10–25 μm as well as smaller ones (in the 2 μm range). The holes appear to define (surround) relatively dense areas with a typical dimension of 40–200 μm and, occasionally, larger and smaller ones.

The size and spatial arrangement of the 10–25 μm holes suggest that they correspond to locations of original interparticle voids. The 40–200 μm relatively dense areas may then correspond to original 30–60 μm particles or their multiples through a coalescence process involving interparticle cross-linking and incorporation of other solid components of the precursor paste to the granules. Actually, most of the observed 40–200 μm entities may be a result of coalescence, considering that the observed cross sections do not, in general, include the center of the particles.

The 1–3 μm holes found in the bulk appear mainly in the vicinity of larger ones, while a significant portion of the dense areas (particles) appears free of such holes. It is reasonable to assume that the 1–3 μm holes appear in locations of the interparticle material and may have been generated through gas escape and local densification processes, under fixed total volume constraints.

3.1.b. The Membrane Skin

The membrane skin originated from a resin solution precursor, and, therefore, no openings analogous to the interparticle voids of the bulk are to be expected. Still, the bulk of the membrane contains a second population of holes (1–3 μm) not directly associated to the original form of the precursor resin, while SEM and SANS do not indicate the presence of any corresponding entities (holes in the micron or submicron range) in the skin material. In addition, a quite low value of κ_g is found experimentally for the skin.[19,20] The structural factor κ_g is expressing the ratio D_{exp}/D_{cyl},

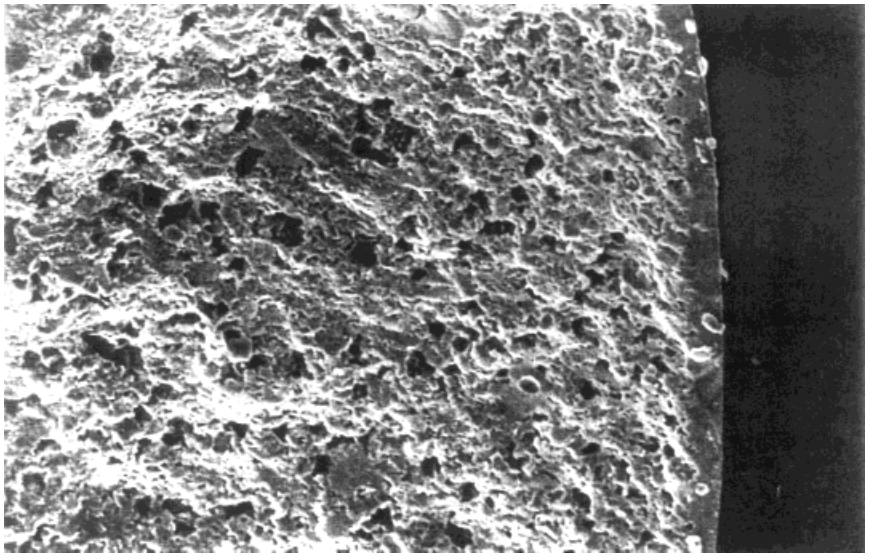

Figure 3 SEM photograph in cross section. The skin (right and outer part of the structure, approximately 50 μm thick) has a compact appearance, while the bulk of the membrane contains various 10–25 μm holes, as well as smaller ones (1–3 μm).

where D_{cyl} is the theoretical diffusion coefficient for a model material having an equivalent cylinder radius = $2\varepsilon/A$ (ε and A are, respectively, the porosity and pore surface area of the real material), and D_{exp} is the experimentally found diffusion coefficient for the real material.[21,22] The κ_g value for the skin replica is on the order of 5×10^{-5}, while its value for model isotropic materials having uniform straight cylindrical pores in three perpendicular directions is $\frac{1}{3}$. κ_g values $\ll \frac{1}{3}$ may be attributed to the following, nonmutually exclusive factors: (1) the presence of constrictions controlling mass transport at the entrance of the pores, and (2) very large sample tortuosity (i.e., diffusion requires excessive tortuous paths). In either case, a very low κ_g value is incompatible with the presence of macropores playing a significant role in transport of the unactivated membranes.

Even if present, the volume fraction of macropores is very low, and their shape and arrangement is very far from forming continuous paths for lengths comparable—within two orders of magnitude—to the skin thickness. Significant extents of macroporosity (e.g., 5%) with continuous macropore paths traversing the membrane skin can form only upon very extensive membrane activation (see Section 3.2.b). A schematic of the skin and bulk global structure of the membrane appears in Figure 4.

The absence of macroporosity in the skin may be attributed mainly to the special characteristics of the skin carbonization: the skin material is made from a solution precursor; and, further, it is located at the exterior of the membrane. Hence, the skin undergoes the carbonization reactions first; also, this is done in the presence of a free surface. As a result, the skin material has the freedom to pack more efficiently, while the interior (bulk) undergoes structural changes under dimensional constraints (as the skin hardens, the tube diameter becomes fixed). Consequently, the bulk material (and especially, the less-dense or less-rigid interparticle material) preserves or develops macroporosity, while the skin becomes compact at the micron scale. It may be noted that a dense, relatively featureless skin also develops

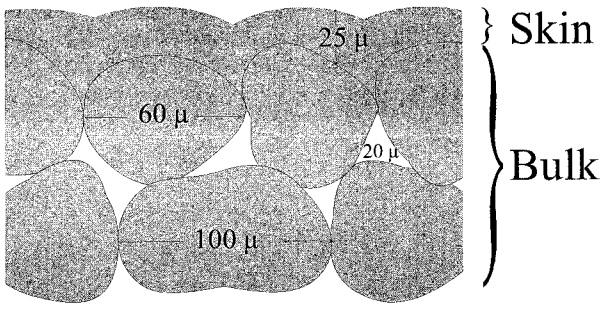

Figure 4 A schematic of the global structure of a carbonized asymmetric membrane. The skin has a (nearly) compact appearance, while the bulk includes 10–25 μm holes.

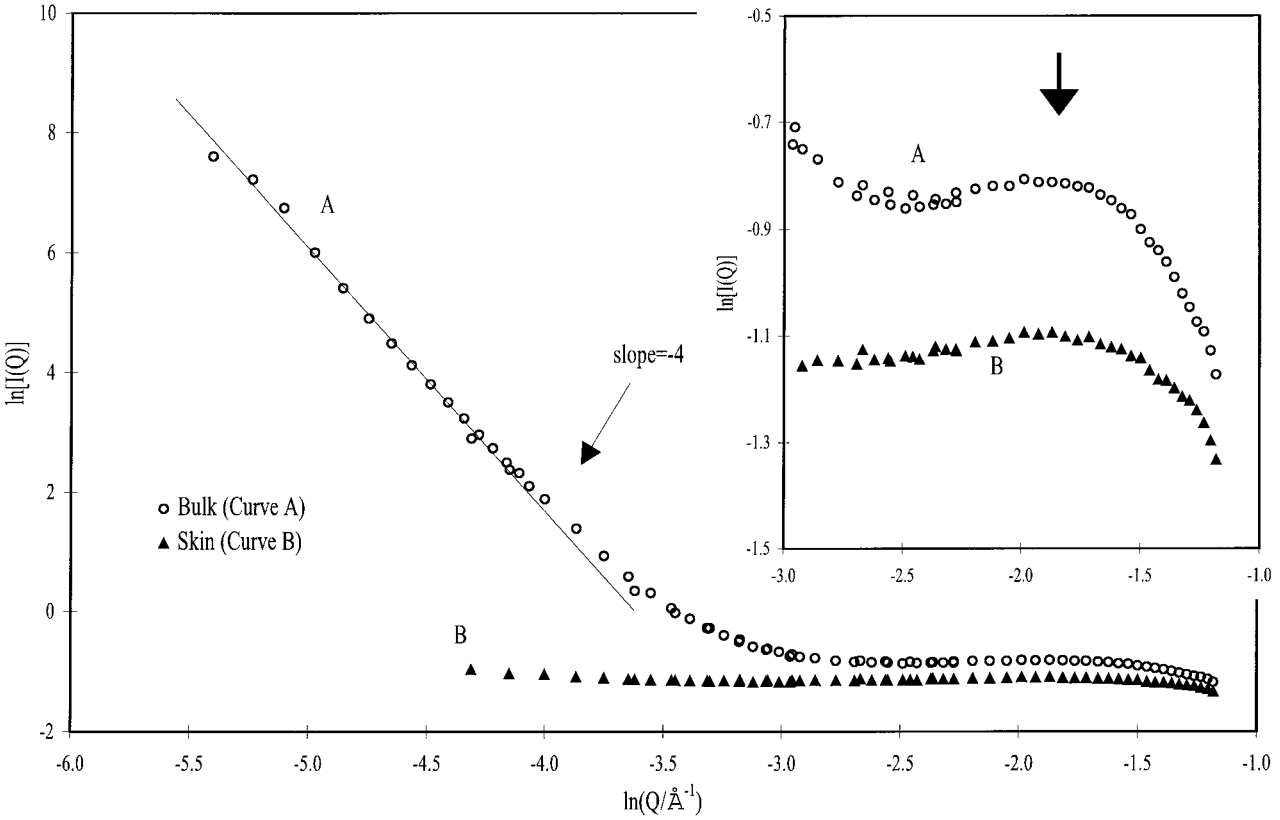

Figure 5 Porod plots for the bulk of the membrane (Curve A) and the skin replica (Curve B). A straight line with a slope of −4 (Porod's Law) is also drawn. The insert shows the details of the regime where the peak is located (at approximately 0.0157 nm^{-1}).

in various other cases, as, for example, in the exterior of polymeric fibers[23] and membranes,[24] prepared through coagulation of a polymer solution. Such cases may be considered, broadly, as examples of a crust formation process occurring widely in nature when a material with a free surface undergoes structural changes progressing from the surface to the bulk.

3.2. Local Membrane Structure

3.2.a. Main Structural Features

In this section, we will present a working model for the membrane bulk and skin, based on the combination of nitrogen adsorption (Section 2.3) and SANS data. The description of the SANS scattering curves will also provide some additional information pertaining to the global structure (Porod's Law regime).

Figure 5 shows the scattering curves for the bulk of the membrane and the skin replica, in the form of Porod plots [log $I(Q)$ versus log (Q)]. In the case of the membrane bulk, the inner part of the curve (low Q values) follows a Porod's Law [eq. (1.4)] with an exponent of 4.0 ± 0.1, whereas the outer part ($Q \geq 0.05$ $Å^{-1}$) approaches a constant value. In addition, the outmost part of the spectrum includes a broad peak.

The form of the scattering curve for the membrane (Fig. 5) suggests that there are more than one type of inhomogeneities, with largely different average dimensions. The fact that $I(Q)$ is found to be proportional to Q^{-4}, even for the smallest scattering angles ($Q = 0.04$ nm^{-1}) where data have been recorded, implies the presence of inhomogeneities large enough for the inequality[25]: $Q \cdot d_{min} \geq \pi$ to hold. Thus, for the corresponding large structural features of the Porod's Law regime, $d_{min} \geq 78.5$ nm (~ 0.1 μm). We have already noted that the bulk membrane material comes from a structure that lost solids after its external

shape became fixed, as a result of skin formation. Such a structure is bound to develop additional structural features (pores and walls between them) at one or more scales in order to compensate for the loss of material. Then, the inequality $d_{min} \geq 0.1$ μm includes structural features seen in the SEM photograph (Fig. 3), described in Section 3.1.a (e.g., 1 μm pores). It may also include additional structural features (pores and walls) belonging to the next, smaller structural scale (0.1–1 μm).

We now return to the issue of scattering from structural features at the local size scale. We will consider that scattering results from inhomogeneities of a characteristic dimension that is close to the corresponding $Q \cdot d_{max}$ limit ($= \pi/6$; see Section 2.2). From Figure 5, we estimate that the scattering from the structural features with $d_{min} \geq 0.1$ μm decays at $Q = 0.5$ nm^{-1} (i.e., the form of the scattering curve is not affected by the large structural features beyond that Q value); then d_{max} should be on the order of 1 nm. By comparing this estimate of the d_{max} value with the results of nitrogen adsorption of Section 2.3, we conclude that the outer part of the spectrum reflects the scattering from the micropores (it may also include contributions from solid structural features of the same size scale). In fact, d_{max} is slightly smaller than the average pore diameter obtained by nitrogen adsorption (1 versus 1.2–1.3 nm); thus, a genuine Guinier region (Section 2.3) may be identified at this part of the spectrum.

The broad peak at the outermost part of the log $I(Q)$ versus log (Q) plot for the bulk sample corresponds to structural entities with a characteristic dimension of approximately 4–4.5 nm, in terms of Bragg spacing. We identify those entities as carbon domains and not as pores because, otherwise, a dominant 4–4.5 nm pore population would have led to different adsorption characteristics of the nitrogen isotherm (possibly a type IV isotherm, characteristic of mesopores). It may also simply be noted that a 4–4.5 nm pore diameter value is in complete disagreement with the experimentally found distribution of pore sizes.

The presence of the above-described peak tends to mask the quantitative details of the scattering resulting from the presence of micropores. Nevertheless, semiquantitative estimates can be made. We have performed a Guinier analysis[12,13] (Section 2.2) of the outer portion of the spectrum and tested the following possible pore shapes: thin discs, long cylinders, and spheres. Our data analysis favors a spherical (or, more broadly, a low asymmetry) pore shape with a radius of 0.5 $\pm$ 0.05 nm, while the other two model shapes lead to negative radii of gyration, having no physical meaning. Figure 6 illustrates this result.

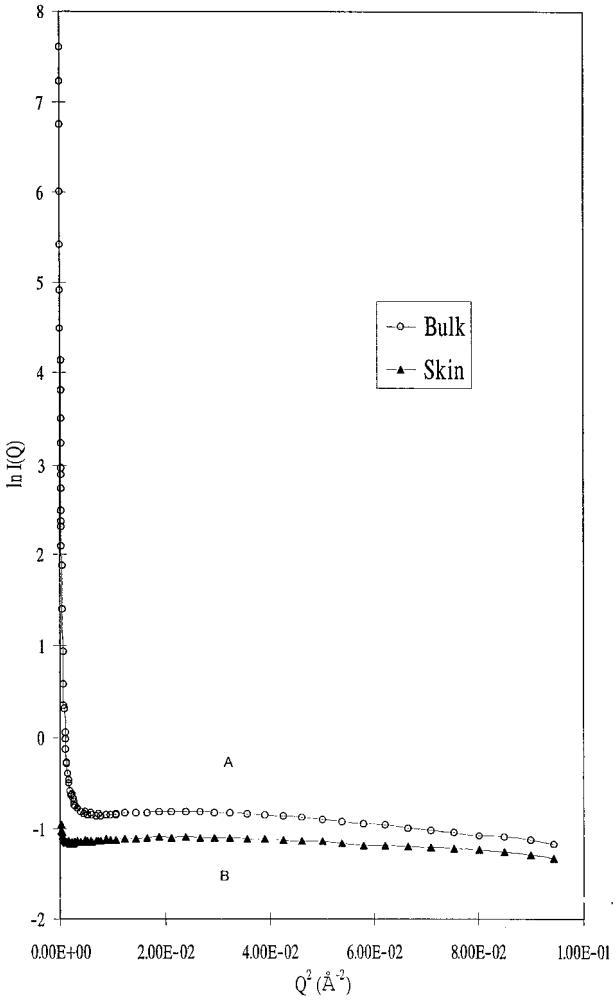

Figure 6 Guinier plots for the bulk of the membrane (Curve A) and the skin replica (Curve B). Guinier fit was applied to the outer part of the spectra (high Q values).

The scattering curve for the skin replica (Fig. 5, curve B) differs from the corresponding curve for the bulk (Fig. 5, curve A) in that it does not exhibit a strong scattering intensity part for the inner part of the spectrum. This difference is due to the previously described (Section 3.1.b) absence of large structural features (solid domains and voids) in the case of the skin replica. On the other hand, curves A and B exhibit similar shapes for the outer part of the spectrum; and the similarity becomes of quantitative character, if one sub-

tracts a straight line (corresponding to the low Q values) from curve A.

We suggest that the bulk and the skin material exhibits similar structural features at length scales below 10^1 nm. The following strong indications support our suggestions, as follows: 1) a shared Bragg peak corresponding to the characteristic dimension of the solid domains, 2) the similar values of the micropore diameters (as estimated by Guinier analysis), and 3) the 0.30 microporosity levels for both the bulk (Table I) and the ground skin replica sample (not shown in the table). Regarding the latter feature, we note that the corresponding microporosity value for the unactivated Sample 1, prepared directly as a powder and not through grinding of a replica crust deposited on a steel plate, is higher (0.38). The difference may be attributed to a slower opening of the pores in the case of bulk objects, as Sample 1 consists of 1–3 μm grains.

We will now consider a simple working model for the local structure: a packing of uniform in size (4 nm) spherical carbon domains. In reality, those domains may be of spherical, cubic, or another similar shape with an aspect ratio near 1. Subsequently, we will discuss this picture in the light of additional available information:

Porosity. Certain features of the proposed arrangement may be compared to those of a random close packing (rcp) of spheres.[26–30] The rcp arrangement exhibits a 0.365 porosity, with pores having a distribution of diameters with a peak near $0.29D$ (corresponding to spherical holes inscribed in the interstices of a rcp arrangement of spheres with a diameter D[31]). Indeed, the microporosity of the material is found to be approximately 0.37 or more (Table I and Section 3.2.b). A porosity above the 0.37 level can be generated in more than one ways; for example, 1) the uniform size spherical entities are not packed in the most effective manner (which may be a result of the domain formation mechanism), and 2) the domain shape is not exactly spherical (for example, a random close packed arrangement of short cylinders or cubes may show porosities in the >0.4 porosity range[32]).

Surface Area. Another test for any structural model is the magnitude of the specific area of the model compared to that of the real material. Low-aspect-ratio compact particles, with a 2.0 to 2.3 g/cm^3 density and a linear dimension of 4 nm diameter, correspond to a specific area of approx. 650–700 m^2/g. On the other hand, the estimate for the unactivated powder simulating the skin is comparable but somewhat larger (750–800 m^2/g, Table I). Actually, the surface area value for a reference material having all of its pores activated is probably in the 1300–1350 m^2/g range (see Section 3.2.c). However, the absolute value of the specific area of porous carbons is often quite unreliable[14] and may be best viewed as a qualitative guide for order of magnitude estimates.

For a microporous carbon, a difference in surface area by a factor of up to 2 (in either direction) is not rare and may simply reflect a deficiency in the methods of assessment. This is because the close proximity of the microporous walls creates problems of both energetic, due to overlapping wall potentials, and purely geometrical nature. Consequences include the possibility of immediate micropore filling, uncertainty regarding the N_2 density value appropriate for the calculations, etc. Within the framework of our model, additional reasons for deviation may be a certain surface irregularity (for example, a waviness that may already be present in the unactivated sample or evolve gradually during activation) and an asymmetry in the particle shape. Consequently, we will not reject any structural model as long as it agrees with a factor of 2 with the experimental value (i.e., we will consider models leading to 650–2500 m^2/g surface areas).

Further, it may be noted that the surface area value for a model structure depends on the dimensions of the compact structural unit and is only weakly dependent on the exact shape of the compact particle and independent of the packing arrangement. For example, we get the same model value for either rcp or loose random packing (lrp) of D diameter spheres; an rcp of D side cubes; or other hypothetical arrangements, such as a packing of cubes containing some slit-shaped micropores and some mesopores. Also, the specific area for spheres with a diameter D differ only by a factor of 0.5 from the value for disks with the same diameter (D) and a thickness of $D/8$. Hence, we may conclude that solid structural units with a 4 nm characteristic dimension are, as an order of magnitude estimates, compatible with the found surface areas. On the other hand, the relative values of the found surface areas are more reliable quantities since the effect of some sources of error (such as the density of the pore filling/covering nitrogen) will cancel out.

Micropores, Porosity, and Random Packing. We have already concluded, from Guinier analysis of the SANS data for large Q values, that the micropores have, most probably, a non-elongated shape. The latter feature is compatible with a random packing of single size domains of near 1 aspect ratio; such a packing should, in general, contain holes with no pronounced asymmetry. However, the particular packing is not the only one containing isotropic pores, and the issue of local scale ($<10^1$ nm) structures compatible with the available experimental data will be discussed in detail in Sections 3.2.d and 3.2.e.

The rcp arrangement having a porosity of 0.365 corresponds to a well-shaken random arrangement of spheres, while the arrangement resulting from simple pouring of uniform size spheres in a container (lrp[33]) results in a porosity of 0.399. The rcp arrangement corresponds to a pore diameter distribution with a peak near $0.29D$ (where D is the diameter of the packed spheres), while lrp corresponds to a peak near $0.40D$.[31] In the case of our sample, upon activation, the microporosity may reach the 0.50 level (Section 3.2.b); while the dimensions of the solid part remain, most probably, nearly fixed.

For an open random arrangement with 0.50 microporosity level, the pore diameter peak will probably shift to values comparable or even larger than $0.5D$. Such pore values appear objectionable for two reasons: 1) they are significantly larger than those determined by nitrogen adsorption and SANS (no larger than $D/3$), and 2) the limits of microporosity are reached or even surpassed (See Section 3.2.d for further discussion).

Regarding the pore diameters used in the above comparisons, it should be mentioned that estimations come from different methods (SANS, nitrogen adsorption, and sphere packing modeling) without a well-established equivalence. Even for the same method, it has been clearly demonstrated[34] that there is a certain degree of arbitrariness (nonunique definition of pore radii) in the case of the sphere packing models, for example, for the same cavity, one may inscribe either two large spheres or three smaller ones. The distributions leading to the aforementioned peak values ($0.29D$ for rcp, etc.) are found with the adoption of a radius-assignment method leading, in general, to the largest of the possible spheres. Hence, differences in method, in combination with experimental uncertainties, may be responsible, at least partially, for the difference in pore diameter values.

In conclusion, an open version of the described model for the local structure is near satisfactory, with certain problems in the porosity-pore size relationship. This and other pertinent issues will be discussed amply in subsequent sections. Still, the sphere packing model will be a valuable guide for the visualization of the additional results and conclusions of the following two sections about the local structure.

3.2.b. Activation of Membranes

The original membranes are normally activated at 800°C in flowing CO_2 for various times. During activation, an amount of carbon is removed (as CO); and it is of technical interest to modify the pore size and porosity in a controllable manner. In order to study the effect of activation on the membrane skin, a powder sample having the same solid contents as the skin precursor is carbonized to a maximum of 800°C. Subsequently, the powder is activated for various times, and the resulting pore size distributions are studied by nitrogen adsorption. It is expected that, during activation, the skin of the actual membranes will show similar structural trends (possibly with a time lag due to a larger characteristic dimension) at the $< 10^1$ nm size level.

Table II provides information regarding the porosity developed during activation of the carbonized powder sample.

L is the weight loss during an activation schedule. V_t is calculated from nitrogen adsorption data and includes all pores below 10–11 nm (practically only micropores, as we have no signs of mesopores). Microporosity ε is calculated as $V_t/(V_t + 1/d)$, where d is the helium-measured density of the compact part. Total porosity ε_t is calculated as

$$\varepsilon_t = 0.38 + (1 - 0.38)\,L \qquad (3.1)$$

where ε_t is a sum of the microporosity of the unactivated sample (0.38) and the additional porosity (of any type) generated during activation. It is assumed that the bulk dimensions of the grains become fixed, following the formation of Sample No. 1. Note that ε_t does not include the following two contributions to the total porosity: 1) macropores (or large mesopores) already present in the unactivated sample; this contribution

Table II Porosity Data[18] for Powder Samples 1–5[a]

Sample	Weight Loss [(L) (%)]	Total (Micro-)pore Volume [V_t (cm^3/g)]	Expected	
			Microporosity (ε)	Total Porosity (ε_t)
No. 1	0	0.297	0.38	0.38
No. 2	6.5	0.360	0.42	0.42
No. 3	10	0.420	0.47	0.44
No. 4	16	0.456	0.49	0.48
No. 5	30	0.523	0.53	0.57

is probably small (and no mesopores can be seen in the isotherm) and, in any case, of no direct importance for the discussion that follows; and 2) blocked micropores present in the unactivated sample. These pores are discussed in more detail below.

Similar values of ε_t and ε may imply that the new open pores generated through activation belong primarily to the < 10 nm range (and, more specifically, in the micropore range, as we have no signs of mesopores in our case). The isotherm of the activated material should then retain the same type of shape as the original material (Type I isotherm). Negative deviations in porosity values (i.e., $\varepsilon_t < \varepsilon$), if not due to experimental errors, may reveal a special population of micropores that were already present in a blocked form in the unactivated material and became accessible upon activation. The activation of those blocked pores is associated to the increase of helium-measured density (from 2.02 to 2.2 g/cm^3 or higher values). However, this density value also increases as a result of a better alignment of the graphitic planes, and the two contributions (opening of micropores and graphitic plane alignment) may not be easily separated in that range of densities.

According to the above description, the ε_t and ε values of sample nos. 2, 3, and 4, in combination with the shape of isotherms (no mesopores), imply that the open porosity generated by activation may be nearly exclusively of the micropore type. Some of these micropores may have been present already, in a blocked form, in the unactivated sample. The volume fraction of the unactivated sample occupied by these blocked micropores may be as low as 3% (sufficient to account for the negative deviation of Sample No. 3) to as much as approximately 5% (if the shift in helium measured density from 2.02 to 2.2 g/cm^3 was to be attributed exclusively to the opening of blocked micropores). Further activation may open those micropores but may lead to new blocking as well. The fall in helium measured density from 2.11 to 2.06 g/cm^3, between samples 3 and 4, may actually indicate the formation of more blocked pores. The new blocked pores (of unspecified type) may then occupy approximately 1.2% (to account for the fall in density) of the volume of Sample No. 4.

Positive deviations in porosity values (i.e., $\varepsilon_t > \varepsilon$) imply that, upon activation, pores on a larger scale (meso and macropores) were formed, along with micropores. According to Table II, Sample No. 5, which has been extensively activated (30% weight loss), falls into that category. The conclusion is also in qualitative agreement with the observation that the full asymmetric membrane has very large gas permeability and no G-S properties when activated under the No. 5 program.

An estimate of the macroporosity of sample No. 5 can be made as follows: if eq. (2) is used with a corrected microporosity of sample No. 1 (0.38 + 0.03 to 0.38 + 0.05, to include the blocked micropores), then a corrected total porosity (ε_t') of 0.59–0.60 is calculated for sample No. 5. Let us now call ε_{mi} and ε_{ma} the microporosity and macroporosity, respectively, of sample No. 5. Note that ε_{mi} will be smaller than ε, as ε_{mi} is pertinent to a volume that includes macropores as well. Then

$$\varepsilon_{mi} + \varepsilon_{ma} = \varepsilon_t' \ (=0.59 \text{ to } 0.60) \quad (3.2.a)$$

$$\varepsilon_{mi}/(1 - \varepsilon_{ma}) = \varepsilon \ (=0.53) \quad (3.2.b)$$

The above equations give a macroporosity value of 0.13 to 0.15 (volume fraction of macropores in sample No. 5).

The extent of macroporosity necessary for the skin to lose its G-S properties will depend both on the shape and the distribution of the macropores.

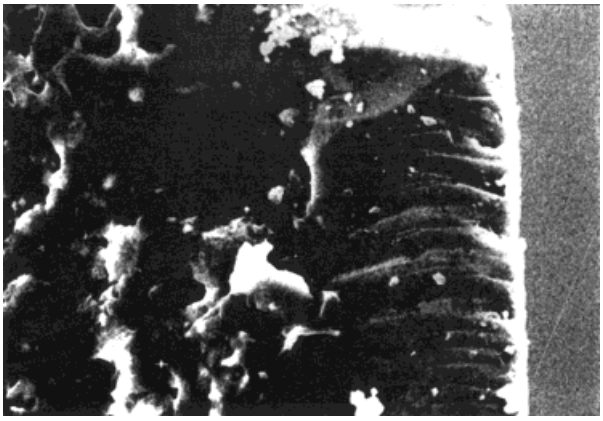

Figure 7 SEM photograph (×625) of an extensively activated membrane in cross section. A set of striations are present in the previously (Fig. 3) compact skin (right and outer part of the structure).

For example, few (e.g., 1% volume fraction) elongated macropores traversing the skin may suffice, while the percolation threshold for randomly distributed spherical macropores is on the order of 16%. However, since the thickness of the skin is only one or two orders of magnitude larger than the macropores themselves (while the external membrane surface is, for practical purposes, infinite), an essentially continuous macropore path may be established, at several locations of the skin, for a lower volume fraction. Hence, the estimated range of macroporosity values for powder No. 5 is probably sufficient for a continuous path of randomly distributed macropores. However, it should be noted the comparison between activated membrane skin and powder sample Nos. 1–5 macroporosities is not very safe beyond the qualitative level. This is because macroporosity features may be strongly affected by the characteristic dimension of the material, the gases which evolve from the substrate (only in the case of skin), etc.

A number of SEM photographs showing longitudinal sections of full membranes indicate the presence of striations crossing the skin, in a direction normal to the membrane surface in the case of extensively activated samples (Fig. 7). While the striations may be simple stress fractures, one should not exclude the possibility that such marks are associated to macropore paths. Still, we cannot estimate a corresponding macropore volume fraction from these photographs and, consequently, draw a conclusion regarding the presence or not of another extensive set of macropores with a more random spatial distribution. Either or both types of macropores may be responsible for the loss of G-S properties in Sample No. 5.

3.2.c. Activation Mechanism and Local Structure

As the size distribution of open micropores for Samples No. 1–4 does not shift to larger values with the increase of microporosity, we consider that the vast majority of the micropores of these samples may belong to one of the following three categories: unactivated, fully open, and (nearly) empty but blocked ones. We exclude, thus, the possibility that a large population of partially activated (smaller diameter) pores exists, considering that the pore size distribution remains the same for samples Nos. 1–4, while the porosity increases. We may now distinguish the following four possible processes of pore formation during activation.

1) Removal of additional disorganized material found in the vicinity of organized compact material (either material fully occupying the future pore space or simply blocking the entrance of certain already formed micropores). This process should generate micropores.
2) Essential enlargement of micropores through corrosion of successive layers of the organized compact material, following the elimination of the majority of the amorphous material.
3) Removal of defective 4 nm domains. This process should generate mostly mesopores.
4) Removal of large accessible clusters of 4 nm domains, leading to the formation of macropores. This process may become possible if the corrosion of domain walls through activation reactions proceeds in limited size areas rather than homogeneously throughout the sample.

As the pore distributions of the activated samples indicate (Fig. 2), activation has not led to any significant changes in the size distribution of the micropores (except for Sample No. 5). Process 1) may indeed increase the open microporosity and the specific area, without really affecting the micropore size distribution. The preference for amorphous and disorganized interparticle material, rather than for the nearly crystalline domains themselves, is not surprising. The intra-

particle material is found at energetically elevated states, and, in general, it is also more accessible as well. In case additional types of pores are formed (as, for example, in Sample No. 5), process 2) may operate. However, process 2) seems to operate in the case of Sample No. 5 but, apparently, in parallel with process (4). Since the formation of a significant population of macropores leads to a complete loss of G-S properties, this route of changing the micropore size cannot be used for the tailoring of a different micropore size G-S membrane. We do not have any direct indication that process 3), or any other mesopore-forming mechanism, operates. This is because the powder samples, both before and after activation, give a shape of isotherms corresponding to microporous materials with no (significant) mesopore contribution. For the same reason, the $V_{0.95}$ porosity of Table I is a microporosity as it does not include any significant mesopore contribution. However, it is reasonable to assume that mesopore-forming mechanisms do operate, especially at some stage following the end of process 1), but the operation is local and not global (i.e., it does not operate simultaneously throughout the sample). As a result, only the final product (i.e., macropores) and no considerable concentration of the intermediate product (mesopores) can be detected.

Another point that merits discussion is the specific area of the membranes. The bulk of the increase in the specific surface area with the extent of activation (Table I) is, clearly, a result of generation of additional open micropores with the same diameter, through new activation or deblocking. In the absence of mesoporosity, the maximum attained surface area is to be attributed, practically exclusively, to micropores; and it may then be compared to our model value for 4 nm particles with a 2.0 to 2.3 g/cm^3 density. Experimentally, we estimate a surface area of 1200–1270 g/cm^3 for Sample No. 4 (the last sample with 1.3 nm diameter pores; Fig. 2) versus 650–700 g/cm^3 for the model particles. As we have noted previously, an agreement of the absolute values within a factor of 2 is acceptable, but other models may also satisfy this condition, as we will see in sections 3.2.d and 3.2.e.

The surface area measurements, while of qualitative only value as absolute numbers, are more reliable as relative values and may actually be used to test ideas regarding the evolution of microporosity. We will assume that the surface morphology of the interface between the activated pore and the carbon domain remains the same for sample Nos. 1–4. We may now note that sample Nos. 1–4 are characterized by an open microporosity (ε), a blocked microporosity (ε_b), and a potential microporosity (ε_p), corresponding to the yet-unactivated material. Up to Sample No. 4 ($\varepsilon = 0.48$; $A = 1{,}269$ m^2/g; $r = 0.65$ nm), activation leads to an increase in open porosity without a significant corrosion of the solid carbon particles (pore size distribution remains nearly the same). On the other hand, corrosion of solid carbon particles has taken place in the case of Sample No. 5 ($\varepsilon = 0.54$; $A_L = 1{,}465$ m^2/g; $r = 0.75$ nm).

A terminal porosity (ε_o) and surface area value ($A_{L,o}$) need to be specified for a reference sample that has been fully activated, without any corrosion of the solid domains. We will use a reasonable set of values as follows: $\varepsilon_o = 0.50$; $A_{L,o} = 1{,}320$ m^2/g. According to our description of microporosity evolution, the following equations need to be satisfied for any of the Samples, Nos. 1–4.

$$\varepsilon + \varepsilon_b + \varepsilon_p = 0.50\ (=\varepsilon_o) \qquad (3.3.a)$$

$$\varepsilon/(\varepsilon + \varepsilon_b + 2\varepsilon_p) = A_L/A_{L,o} \qquad (3.3.b)$$

Equation (3.3.a) is an immediate consequence of the definition of the various ε values. Equation (3.3.b) states that the lower specific areas result from the fact that the surface areas used for the calculation of the specific surface area are only those of the solid domains adjacent to an open pore, while the masses used in the same calculation are those of all solid domains (adjacent to an open pore, or not).

Then, the mass of the solid domains may be viewed as consisting of the following three parts: 1) mass of the solid domains adjacent to the open domains, 2) mass of the solid domains adjacent to the blocked domains, and 3) mass of the unactivated part (which will be approximately twice that of the corresponding solid domains alone, as the terminal porosity is taken to be 0.50). Note that in a refined version of the equations, the difference in density between the densified solid and the amorphous material-filled domains should be taken into account. Table III shows the calculated ε_b and ε_p values for sample Nos. 1–4.

The exact results will depend on the assumed ε_o and $A_{L,o}$ values, and the dependence is stronger for the more activated samples. However, while the cited calculations can be simply viewed as part

Table III Levels of Various Types of Microporosity for Four Activated Samples

Sample	ε	ε_b	ε_p
No. 1	0.38	0.03	0.09
No. 2	0.42	0.03	0.05
No. 3	0.46	0.03	0.01
No. 4	0.48	0.02	0.00

of the demonstration of the method, we may note that for various reasonable ε_o and $A_{L,o}$ values, we have found reasonable ε_b and ε_p values. In particular, we found ε_b values, mostly in the 0.00–0.04 range. In addition, these found ε_b values did not necessarily decrease continuously with an increasing extent of activation, while the ε_p values did. The results of the calculations are qualitatively compatible with the conclusions we drew previously in Section 3.2.b about the presence of blocked microporosity through a different and independent route. Note that the equations used are not bound to produce reasonable results, as they can easily give, for example, large negative ε_p values.

3.2.d. Arrangements of Carbon Domains with Interparticle Porosity

So far, we have established that the material has a reference microporosity in the 0.40–0.55 range (most probably near 0.50), a structural unit with a characteristic dimension in the range of 4 nm, and a smaller dimension on the order of 1–1.5 nm. The latter feature should correspond, though not necessarily in an exclusive manner, to the characteristic dimension of isotropic pores. The reference specific surface area is on the order of 1300 m^2/g, and we will accept models leading to values in the 650–2500 m^2/g range.

In Section 3.2.a, we have shown that the available experimental evidence is at reasonable agreement with an arrangement of low-aspect-ratio 4 nm compact units. Subsequently, we will attempt to locate alternative options or improved versions of that model structure. In the present section, we will survey of arrangements with interparticle; while in the next section (3.2.e), we will discuss the possibility of a dominant intraparticle porosity.

Disk Arrangements. A disk with a 4 nm diameter (D) and an approximate thickness of $D/8$ will fit the surface area data best; but, as we have already noted, qualitative matching between expected and found surface area is sufficient. On the other hand, an acceptable shape for a solid domain should be compatible with the following characteristics (sections 3.2.a and 3.2.b): 1) nearly isotropic pores with a diameter in the $D/4$ to $D/2$ range, and 2) microporosity in the 0.45–0.55 range.

While a large variety of disk arrangements is possible, those consisting of uniform size elements with a pronounced disk shape (e.g., aspect ratio $\geq$ 4 or 5) tend to form isotropic pores for either small (e.g., $<$0.3) or large (e.g., $>$0.7) porosities. On the other hand, the desirable intermediate porosities (0.45–0.55) are achieved easily in the case of packings reducible to ones of low-aspect-ratio units. Subsequently, we describe the most interesting disk packings found for each case.

A type of disk packing that may contain isotropic pores is obtained when successive close-packed layers of disks are arranged so that an opening in the N layer is sandwiched between a disk from the $N - 1$ layer and a disk from the $N + 1$ layer [see Fig. 8(A) for a side view]. As long as the pores remain isotropic (i.e., of comparable size in the three directions), such arrangements will have a porosity near 0.1. Attempts to make the structure more open, i.e., to generate porosities in the 0.45–0.55 range, appear to either create an additional large population of asymmetric pores (slit or cylinder shaped), require a very small particle asymmetry ($\geq$2), or become nearly equivalent to a packing of low-aspect-ratio units (see below for a related example).

An interesting type of packing that satisfies 1), but tends to give rather large porosities, is based on a regular tetrahedron structural cell [Fig. 8(B)]. The pore can be a small tetrahedron void inside a larger tetrahedron. In addition, the arrangement may allow for pores to communicate, by using smaller shapes for the four walls. An example of a smaller wall shape is a truncated cone having its cross sections inscribed in the triangular cross sections of the full walls. Calculated porosities for the two examples of wall shapes appear on Table IV.

The results in Table IV suggest that if some pore interconnectivity is present (as in the case of the real sample), the aspect ratio necessary for a 0.45–0.55 porosity would be, at best, in the range of 2 : 1. Hence, the description of low-aspect-ratio ($\leq$2) structural units remains adequate.

Finally, an example of a disk arrangement that

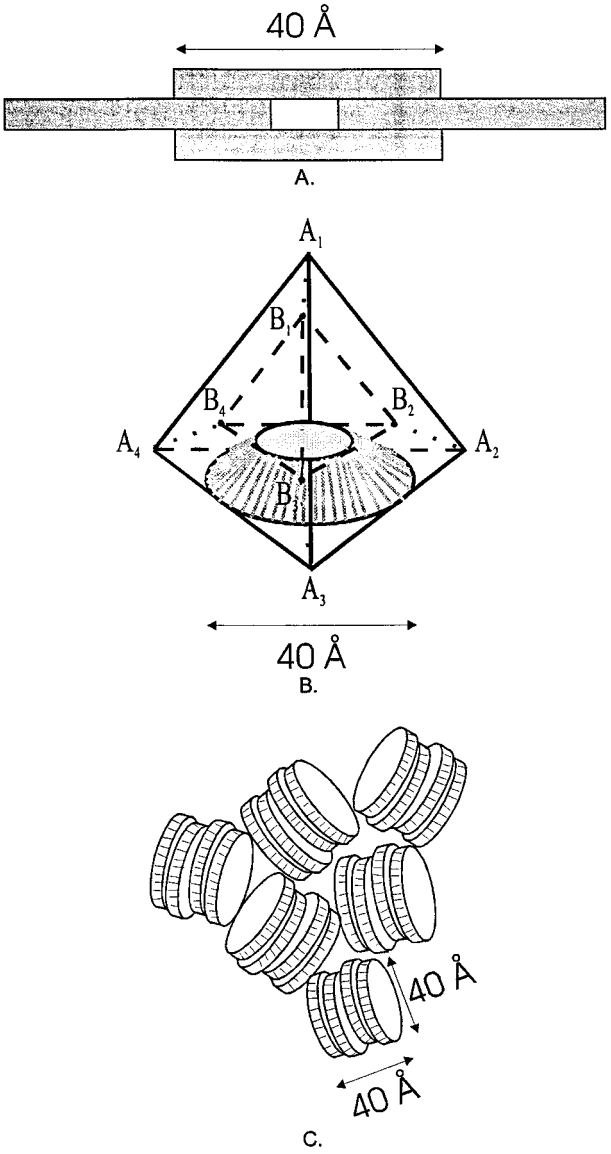

Figure 8 Various disc arrangements. (A) Layered, low-porosity arrangement. (B) Model tetrahedral arrangement: $A_1A_2A_3A_4$, basic tetrahedron; $B_1B_2B_3B_4$, tetrahedral pore. Also shown is a truncate cone representing a bottom wall, allowing pore communication. (C) Stack of discs arrangement.

does satisfy 1) and 2), but is nearly equivalent to a packing of low-aspect-ratio units, appears on Figure 8(C). The disks are arranged in low-aspect-ratio stacks, which are nearly equivalent, in terms of shape, to short solid cylinders. However, this arrangement can be made to possess special features, if we assume narrow (with a width $\leq 0.6-0.7$ nm) slit or wedge-shaped openings located between the discs, capable of filling with nitrogen during adsorption experiments. Such micropores may be undetectable by SANS because they are too small. Figure 2 does not indicate the presence of such pores, but the curves shown are based on the assumption that the pore size distribution is unimodal. Such small anisotropic micropores, if present, may only have shifted the peak of the distribution of the larger isotropic micropores to smaller values. An arrangement of low-aspect-ratio units, including contributions from small slits, cracks, crevices, etc. (or an arrangement of stacks of disks), is an improved version of the working model of Section 3.2.a. This is because such an arrangement can generate extra microporosity (and also extra surface area) without bringing the 4 nm low-aspect-ratio domains further apart from, e.g., an rcp or lrp type of arrangement. The same holds true for low-aspect-ratio cylinders containing wedge-shape pores in a radial or other arrangement. Finally, we should note that the characterization of the additional small, anisotropic micropores as interdomain or intradomain will be more a matter of convention than one of practical significance.

Returning now to arrangements of isolated disks (no stack formations), we should note that for statistical reasons, it is the thickness of a disk, rather than the diameter of it, the dimension that stands a better chance to give a pronounced peak in the scattering intensity. If, however, the diameter of the disk is larger than 2×4 nm, the corresponding specific area will be well outside the acceptable range of 650–2500 m^2/g. The above suggests that the arrangements of units with a pronounced disk shape are less probable candi-

Table IV Relationship Between the Aspect Ratio and the Porosity for Two Flat Wall Shapes in a Model Tetrahedral Arrangement

Wall Shape	Aspect Ratio	Porosity
Full wall	8 : 1	0.82
Full wall	3 : 1	0.58
Full wall	2 : 1	0.42
Truncated cone wall	8 : 1	0.89
Truncated cone wall	3 : 1	0.75
Truncated cone wall	2 : 1	0.65

Notes regarding the aspect ratio calculation: (1) the wall thickness has been doubled, to account for the wall of the adjacent tetrahedron; (2) for an equilateral triangle with a side L, the characteristic dimension used is the diameter of the inscribed circle ($L/\sqrt{3}$).

dates than low anisotropy unit arrangements (with the exception of the low anisotropy stack configuration). However, it is conceivable that a disk arrangement with a medium porosity and elongated pores with an acceptable diameter can be turned into a satisfactory system through the splitting of the elongated pores into small isotropic pieces by minor structural details. We will consider that case, in its general form, later in this section.

Continuous Solid Arrangements. Another general type of candidate structural models is that of an essentially continuous solid (at least one of the dimensions is orders of magnitude larger than D), interwoven with an essentially continuous network of pores. If the solid-void interface is comparably concave and convex, then the cube of the ratio of characteristic dimensions (diameters) of the void and the solid part will be quite representative of the relative volume fractions. This implies a maximum of porosity of $(0.5)^3/(1 + (0.5)^3) = 0.11$. Some caution is necessary regarding the meaning of the characteristic dimension of the solid and the void part obtained by various measurements. The above calculation of an 0.11 maximum porosity is made with the assumption that the available domain and void measurements provide the average length of chords passing through the center of the solid or the void domains. This case is, for example, quite different from the superficially similar looking case of a structure characterized by an 1 : 0.5 ratio of the total lengths that a random in-direction probe spends, respectively, in the solid and the void part of a material. In such a case, the porosity will be on the order of $0.5/(1 + 0.5) = 0.33$. The latter result comes from stereology and is independent of the shape of void-solid interface, etc.

Returning now to the standard considerations of characteristic dimensions (i.e., assume that they represent some type of diameter of a corresponding spherical entity), we note that if the void contour is much more convex than concave, then the maximum possible porosity will take an even smaller value than 0.11. Another comment is necessary here. The 0.11 porosity limit implies that there is the same number of solid entities with dimension D and void entities with a $D/2$ dimension, which is not necessarily true. Now, if the solid part is comparably or less concave than the void part, then the number of void entities should be at least seven times that of the solid entities in order to achieve a porosity in the expected range (0.45–0.55). This can be achieved, for example, with thin walls that may emanate from the main mass of the solid and split the void space into smaller compartments. A general discussion of the issue of compartmentalization can be found in the section entitled "Most Probable Structures" (to follow). In conclusion, unless the void space is further compartmentalized, a level of porosity > 0.45 indicates that, for the structure of interest, the void contour is strongly concave and the solid contour is strongly convex. However, such a structure may then be essentially reduced to discrete solid particles (spheres, disks, etc.) and their interparticle space. For that case, we have already concluded that among solid uniform size particles, the low-aspect-ratio units are the strongest candidates.

Regular Versus Random Arrangements. A general point should be made regarding the relationship between the interdomain pore size and the regularity of the domain arrangement. If the arrangement of 4 nm particles is a seriously disordered one (random in some sense), it is quite possible that the arrangement with a 50% porosity will include a considerable population of large pores having a characteristic dimension in the 2–4 nm range, especially if the average pore diameter is larger than approximately 1.5 nm. Such large pores should have probably led to isotherms with hysteresis characteristics, typical of mesopores. On the other hand, the arrangements with some regularity [not necessarily as ordered as the model tetrahedral arrangement of Fig. 8(B)] appear as more satisfactory candidates than their random counterparts (or other random arrangements, such as lcp, etc.), as long as the pore diameter is under 2 nm (maximum size of micropores). Among regular sphere arrangements,[35] the one possessing a porosity near 50% is the simple cubic one; each sphere is in contact with six spheres, two in each of three perpendicular dimensions. The porosity of this arrangement is 0.48. The pores have a diameter of 0.73 D, but they may only be accessed through pores with a 0.42 D diameter. However, most probably, such an arrangement should lead to hysteresis effects, as the limit of 2 nm corresponds to a $0.5D$ diameter.

Another important issue is that of the microporosity level. In the case of random packings, a single size of carbon domains contributes significantly to a high microporosity value (in general,

$\varepsilon > 0.37$). On the other hand, as a simple calculation shows, a random close packed arrangement of two populations of spheres differing widely in size (so that the small ones can populate the interstices of the arrangement of the large ones) may exhibit a porosity in the 0.14 range, while the corresponding porosity for a single rcp population is 0.37. In the case of regular packings, a single domain size does not lead, in general, to large microporosities; spheres, cylinders, and cubes may pack with porosities as small as 0.26, 0.09, and 0, respectively.

The packing of domains may be more open than predicted on the basis of shape, size distribution, and type of organization (regular or random) of the domains. The reasons for the generation of more open structures should be sought in the details of the formation mechanism (e.g., density adjustments under total volume constraints at the local scale, reorganization restrictions due to certain interdomain connections, etc.).

Structures with D/*3 Pores.* We have previously required that the pore diameter should be in the $D/4$ to $D/2$ range. We have also seen that arrangements having an $\varepsilon \approx 0.50$ and a comparable (within a factor of 2 or 3) number of pores and D-sized domains cannot easily exhibit a pore size smaller than $0.4-0.6D$. While such pore sizes overlap with our acceptable range, we may note that the set upper limit was simply that of microporosity, while pore diameter values found by two experimental methods were considerably smaller (approximately equal to $D/3$).

As we have also noted previously, a way of tailoring smaller pores is through compartmentalization of the interdomain space, by entities such as thin graphitic strings and walls. This construction, however, will also circumvent previous arguments, which led to the rejection of certain options, assuming a comparable number of solid and void entities. We may also note that the idea in its most general form, with pore dimensions determined primarily by the location of small amounts of interdomain material, is somewhat questionable on physical grounds. This is because of the implied requirement that thin graphitic walls and strings will remain nearly intact, while amorphous regions containing one or two orders of magnitude more material will be eliminated. As the relative oxidation rates are only an order of magnitude different, this would require that the amorphous regions themselves will behave as loose groups of strings or walls (i.e., the amorphous material is not compact at the 0.5–1 nm scale).

If the nitrogen adsorption and SANS estimated values of pore diameters are realistic ones (and not underestimates), then an arrangement leading to 1.3 nm diameter pores without making excessive use of additional strings and walls should be a serious candidate structure. One such arrangement is the following: Solid domains with a linear dimension of D (or somewhat larger) and a near cubic shape are packed rather well, and their surfaces bear a dense pattern of near spherical pores. Those pores have a diameter of $D/3$ and are shared with the adjacent cubes [Fig. 9(B)]. Each surface of the solid domain may be thought as bearing an "egg-case" type of arrangement of hemispherical pores. If the arrangement is a very dense one, the microporosity will be near $\frac{2}{3}$. On the other hand, the porosity for an arrangement, which includes solid areas of $D/3$ size between the pores, will be near $\frac{1}{3}$. If structural features detectable by SANS with a characteristic dimension other than $D/3$ are to be avoided, some combination of the two types is necessary for a porosity of 0.50. However, it is dubious if SANS can "see" the small surface solid domains as entities separate from the bulk of the 4 nm domain. In any case, other roughly isotropic surface domain shapes (holes and solids) can also lead to the desired match of values. We may also note that such a type of geometry appears capable of generating very high tortuosity values (Section 3.1.b), especially when a fraction of the micropores (unactivated and blocked) does not participate in transport. This structure differs from those capable of achieving a $D/3$ pore size based primarily on sets of graphitic walls and strings in that most of the pore contour is part of the bulk part of the solid domains. As a result, the pore diameter can remain essentially unchanged in size, even if the narrow parts are thinned down considerably during activation.

Most Probable Structures. In conclusion, the strongest candidates among the packings of a single type of solid domains with interdomain porosity are as follows. (1) A dense arrangement of near cubic domains, bearing a surface pattern of 1.3 nm diameter micropores. The surface area will be in the range of 2000 m^2/g. (2) An arrangement of low-aspect-ratio domains, preferably with additional small intradomain asymmetric pores or

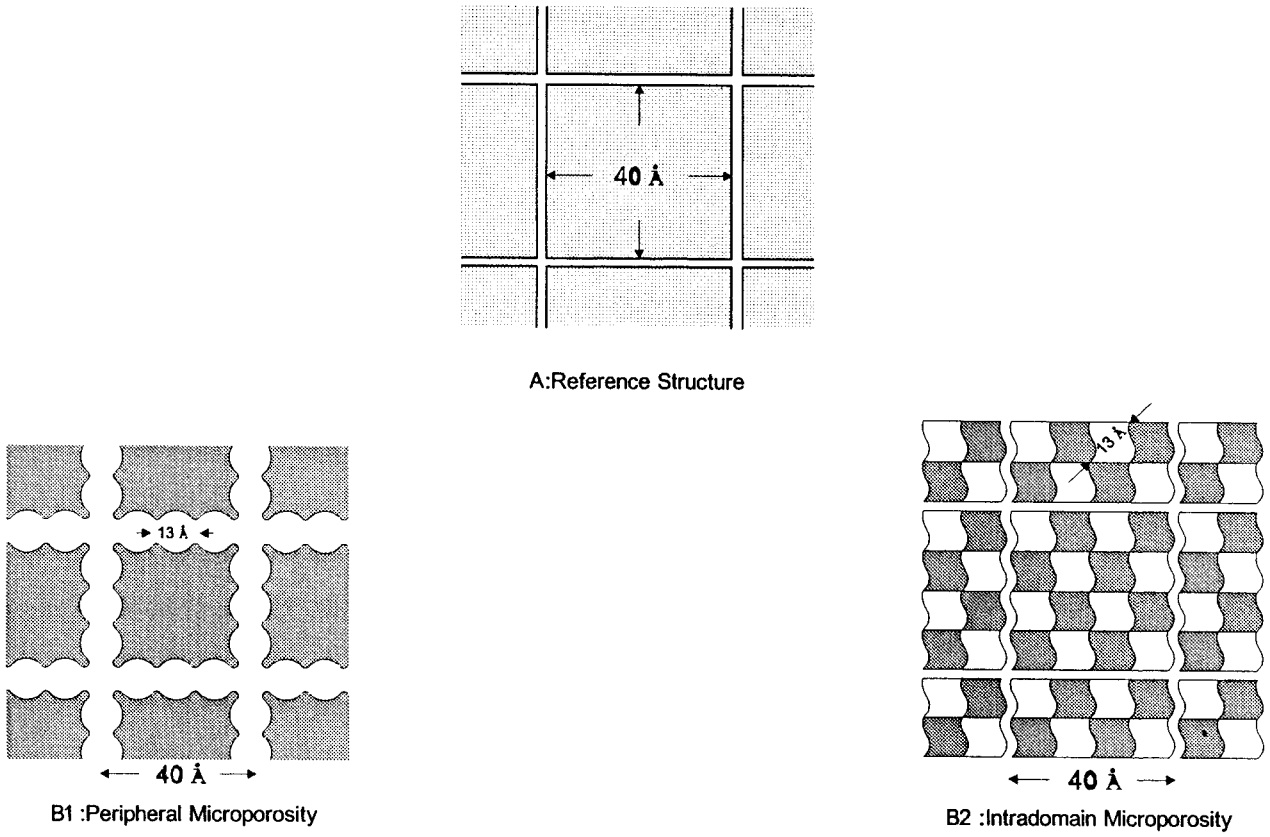

Figure 9 Cross-sectional view of the evolution of microporosity in a dense packing of 4 nm (40 Å) block domains (A). (B_1) Development of peripheral microporosity–"egg case" surface pattern. (B_2) Development of intradomain microporosity.

some surface waviness. The specific surface area will be in the 700 g/cm^3 range for the simple version and in the 1000–2000 g/cm^3 range in the case of the additional structural features. For the plain model, the average pore size will be near 2 nm, and a regular arrangement may be necessary, in order to avoid mesoporosity characteristics. In the case of additional small anisotropic micropores, the larger isotropic micropores may have an average dimension well below 2 nm (e.g., 1.2–1.5 nm); thus, a regular or quasi-regular arrangement of the domains may not be necessary.

Of some interest are arrangements exhibiting 1.3 nm pore domains as a result of compartmentalization of void space by a network of graphitic strings and walls.

3.2.e. Arrangements of Carbon Domains with Intraparticle Porosity

We will focus on a model that has a lot in common with the cube arrangement with the "egg-case" type of surface pattern of the last section [Fig. 9(B_2)]. Again, the reference 4 nm domains have a near cubic shape, and they are relatively well packed (interparticle porosity ≤ 0.1). The intradomain space is split into a pattern of alternating dense and empty areas with a characteristic dimension near $D/3$ [Fig. 9(B_2)]. Such a structure may also have a porosity near 0.5 and a specific area on the order of 2000 m^2/g; hence, it is an equally strong candidate with the related structure of the previous section.

We intend to address quantitatively the interdomain versus intradomain porosity question in a future study. However, we may note that the first candidate arrangement of the previous section (interdomain porosity with an "egg-case" pattern) has a partial two-dimensional character (a significant fraction of the pores will be characterized by two-dimensional connectivity). On the other hand, the second candidate of the previous section (low-aspect-ratio domains with large in-

terparticle micropores) and the arrangement with intraparticle porosity of this section are purely three-dimensional ones. The very low structural factor κ_g of the unactivated membranes (Section 3.1.b) can be a result of the presence of constrictions or a very high tortuosity factor. Unless the very low κ_g value is nearly exclusively due to the first factor, the unactivated membrane should be characterized by high tortuosity. The latter indicates that the pore structure, with an open skin microporosity equal to 0.30, is not well above its percolation threshold.[36] Since the percolation threshold is typically on the order of 0.5 and 0.15, for two and three dimensions, respectively, the arrangement with the "egg-case" surface pattern seems to be the most satisfactory of the three candidates in the high tortuosity case (and it is also capable of generating constriction effects).

We have kept most of our general descriptions in previous sections compatible with both intradomain and interdomain porosity. However, in some instances (e.g., Section 3.2.a), the descriptions refer explicitly to intradomain porosity because we considered that a more specific model will convey an idea better than a more general, but abstract picture. The description of Section 3.2.b is independent of the location of the microporosity. Section 3.2.c refers occasionally to the intradomain case only, but the equivalent descriptions for the interdomain case are rather obvious.

The presented systematic analysis of structures compatible with a microporous carbon of medium porosity should not be viewed as an exercise in imagination. The polymeric materials have been found to possess an incredibly rich variety of structural features at all size scales (see, for example, Bassett,[37] for special cases, see Baer et al,[38] Beltsios and Carr,[23] and references therein). Carbonization may, in principle, preserve the polymeric structural features in some derivative form or generate an even richer variety. Consequently, we felt it was necessary to examine systematically a wide variety of structures and present an analysis of broader interest, rather than adopt directly an existing model for an apparently similar case. On the other hand, we have avoided the enumeration of arrangements containing particles of two or more distinct shapes, with a comparable characteristic dimension (e.g., $L_1/L_2 \leq 2$). The case of a single phase concurrently forming more than one distinct morphologies, at the same size scale, while not impossible,[39,40] is quite rare and was not considered. This should be clearly distinguished from the rather common case of more than one type of opening at the same size scale. More than one type of opening is, for example, commonly encountered in ordered arrangements of spheres (more than one type of interstitial sites) and also in various cases of disc packings, some of which were analyzed in this section. In the latter case, the multiplicity may be often a direct or indirect result of the existence of two characteristic dimensions of the solid domain itself.

3.2.f. Origin of the Domains and the Micropores

The purpose of this section is to show the existence of some plausible physical routes capable of generating the structural features described in the previous sections. We should note that while novolac and resole polymers are both phenol-formaldehyde type resins, they differ considerably in their chemical details. As the two materials upon identical carbonization conditions lead to structures with similar geometrical features, our descriptions emphasize the geometrical and not the chemical aspects of conversion.

The 4 nm diameter of the carbon domains may be a direct descendant of structural features found in the precursor polymers. In particular, this dimension may correspond to a somewhat larger dimension, characteristic of the local packing arrangement of the chains of the amorphous precursors [Fig. 10(A)]. The size of areas between bends (encircled areas) will be related to the ability of packs of chains to bend and the need for satisfaction of space-filling requirements (no large spatial variation of density at the 1–5 nm level for flexible polymer chains). For flexible chains, those requirements appear to be satisfied most easily when the areas between bends [Fig. 10(A)] have a relatively uniform size and a low aspect ratio (i.e., 1 to 2).

During carbonization, the local packings of chains can end up possessing local crystallinity through a succession of organization procedures that include formation of planar arrangements and elimination of the majority of noncarbon atoms. The remaining material (that of the bends, as well as of strongly entangled chain material) will be at energetically elevated states (due to bending, stretching, etc.), and it will also be of lower density and thus more accessible to oxidizing species. As a result, most of this additional material will be preferably eliminated during the

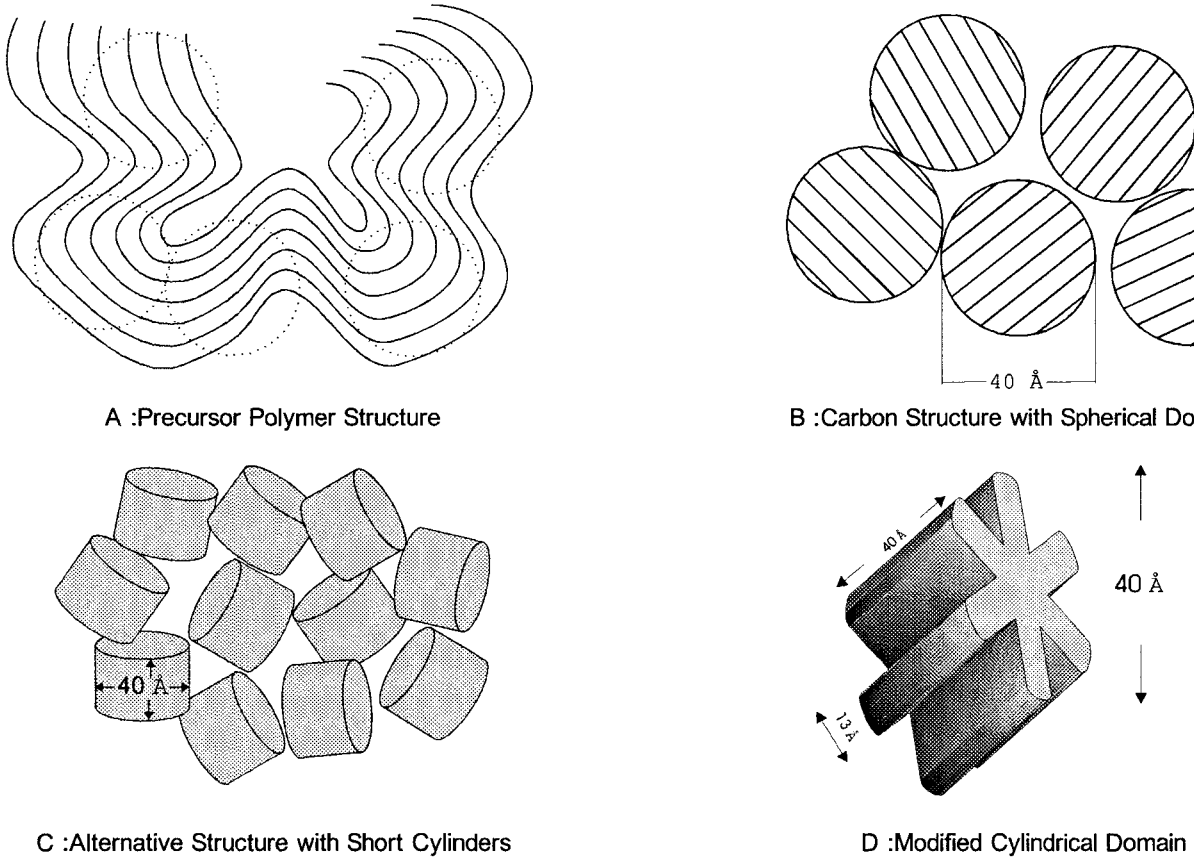

Figure 10 A two-dimensional schematic of the packing of the precursor polymer chains (A). The actual precursor also includes cross-links not shown here. The material in circles may eventually develop into spherical carbon domains (B). Alternatively, a packing of low-aspect-ratio cylinders with isotropic micropores may form (C). A modified low-aspect-ratio cylindrical unit (D) will be a source of additional, wedge-shaped, small micropores.

carbonization and micropore formation procedures [Fig. 10(B)].

Figure 10(B) also shows that close packing is obtained only after some positional rearrangement that may not necessarily take place (leading, in such a case, to porosities > 0.4). Still, the spherical shape is adopted in Figure 10(A) and (B) for simplicity, and other domain shapes of low aspect ratio (e.g., cylinders, cubes or discs, with an aspect ratio ≤ 2) are possible as well. Figure 10(C) shows an arrangement of low-aspect-ratio cylinders. A near cylindrical shape of units may also be produced from a Figure 10(A) type of arrangement. In that case, the chain bundle splits, upon carbonization, into chunks without the implied rounding necessary for the formation of the Figure 10(B) spheres. It is also possible that, upon carbonization, the encircled areas will not separate from each other (at least completely), leading to lower porosity structures, approaching, to different degrees, the familiar model for the glassy carbon.[41]

In the case of structures consisting of 4 nm low-aspect-ratio domains, the porosity may simply represent the space between these domains. However, all three strong candidate structures (two with interdomain and one with intradomain porosity) possess pores in a special arrangement. Subsequently, we will outline processes capable of generating such arrangements.

The two arrangements containing numerous (many more than the solid domains) isotropic 1.3 nm pores (sections 3.2.d and 3.2.e) may be a result of necessary adjustments, when the evolving carbon domains get gradually closer, under the constraint of a nearly fixed volume at the local

($<10^1$ nm) scale. In the first case, densification may proceed from the interior of the 4 nm domains (through some type of nucleation process), leading to a strong surface waviness [Fig. 9(B_1)], plus disorganized material. The latter will be eliminated during activation.

In the second case, the densification may proceed from the exterior of the 4 nm domains; and, upon formation of a rigid case, the interior will split into dense organized areas and areas that will eventually become micropores [Fig. 9(B_2)]. It should be noted that the cubic shape is not a necessity and other low-aspect-ratio shapes (such as short cylinders) may be appropriate as well. Nevertheless, certain restrictions apply. In the case of the model with intradomain porosity, the basic carbon domain shape should be capable of near-space filling ($\varepsilon \leq 0.1$; i.e., it may not have a shape very close to that of a sphere). The corresponding model with a peripheral interdomain porosity can accommodate more surface curvature in the basic domain. However, the more spherical the domain contour, the more vulnerable to oxidation the pore walls may be, with the model approaching that of an open arrangement of spheres with a compartmentalized intradomain space. Finally, the details of the arrangement of the interdomain micropores should be such that a significant portion of them will be characterized by a two-dimensional type of connectivity.

Small, intradomain, slit or wedge-shaped micropores (present simultaneously with the larger interdomain isotropic micropores) may form either as a result of a packing rearrangement of flat units or as a result of splitting of low-aspect-ratio units. The latter case can be realized in case all carbon planes of the same domain are parallel to a certain direction (such as that of the precursor polymer chains). Then, the intradomain densification may generate small slit-shaped micropores parallel to each other, or small wedge-shaped macropores in an arrangement with radial symmetry [Fig. 10(D)].

In conclusion, in this section, we have outlined plausible physical chemical routes, not necessarily the only ones possible, leading to products compatible with the described structural features (domains and micropores) of the solid structure.

4. CONCLUSIONS

A study of the structure of an asymmetric carbon membrane is presented with the help of SANS, nitrogen porosimetry, and SEM data. Under the same carbonization conditions, the phenol-formaldehyde resins of the bulk and the skin lead to structures having the following similar structural features at the $< 10^1$ nm scale: 1) low-aspect-ratio carbon entities with a diameter of approximately 4–4.5 nm, and 2) a porosity of 0.30–0.50 with isotropic cavities of a 1.2–1.3 nm diameter.

The question regarding the exact location of the micropores has not been answered definitely; but according to the strongest candidate model, the micropores are arranged in two-dimensional arrays located at the periphery of the 4 nm domains.

No mesoporosity is present either in the bulk or the skin. Regarding macroporosity, some interparticle macropores (10–20 μm scale) are preserved in the bulk, and some additional macropores (0.1 μm scale) are generated during carbonization. In contrast, carbonization does not lead to any significant extent of skin macroporosity, and the membranes are appropriate for gas separation applications. The gas permeability of the asymmetric membranes may be improved without a loss of the gas separation properties if an activation of a limited extent (e.g., a weight loss of 6%) is applied to the carbonized products.

We thank Mr. R. Soria of SCT for providing us with membrane materials and a variety of pertinent information and Mr. F. K. Katsaros (NCSR Demokritos) for the nitrogen adsorption data of Table I pertaining to the activated carbon replicas of the membrane skin. We also thank G. Charalambopoulou, A. Koutsou, and K. Tzevelekos (NCSR Demokritos) for contributions in the experimental section and/or useful discussions.

REFERENCES

1. J. Gregg and K. S. W. Sing, *Adsorption Surface Area and Porosity,* 2nd ed., Academic, London, 1982, p. 25.
2. K. S. W. Sing, D. H. Everett, R. A. W. Haul, L. Moscou, R. A. Pierotti, J. Rouquerol, and T. Siemieniewska, *Pure Appl. Chem.,* **57,** 603 (1983).
3. W. Watt and W. Johnson, *Appl. Polym. Symp.,* **9,** 215 (1969).
4. K. Beltsios and J. Economy, Unpubl. data on graphitic BN and C fiber processing.
5. R. Bacon, *Phil. Trans. Roy. Soc. Lon. Ser. A.,* **294,** 437 (1969).
6. W. Johnson, *Nature,* **279,** 142 (1979).
7. R. Bacon and W. A. Schalamm, *Appl. Polym. Symp.,* **9,** 285 (1969).

8. E. Fitzer, *Angew. Chem. Int. Ed. Engl.,* **19,** 375 (1980).
9. A. Ch. Mitropoulos, J. M. Haynes, R. M. Richardson, and N. K. Kanellopoulos, *Phys. Rev. B,* **52,** 10035 (1995).
10. I. Simitzis, J. Sfyrakis, A. Faliagas, *J. Appl. Polym. Sci.,* **58,** 541 (1995).
11. U. Keiderling and A. Wiedenmann, *Physica B,* **213,** 895 (1995).
12. A. Guinier and G. Fournet, *Small Angle X-ray Scattering,* Wiley, New York, 1955.
13. G. Porod, *Small Angle X-ray Scattering,* O. Glatter and O. Kratky, Eds., Academic, New York, 1982, Chap. 2.
14. J. Gregg and K. S. W. Sing, *Adsorption Surface Area and Porosity,* 2nd Ed., Academic, London, 1982, Chap. 4.
15. M. M. Dubinin and V. A. Astakhov, *Adv. Chem. Ser.,* **102,** 69 (1971).
16. P. J. M. Carrott, K. S. W. Sing, *Characterization of Porous Solids,* K. K. Unger et al., Eds., Elsevier, Amsterdam, 1988, p. 77.
17. S. Lowell and J. E. Shields, *Powder, Surface Area, and Porosity,* 3rd ed., Chapman and Hall, London, 1991, Chap. 9.
18. M. M. Dubinin and L. V. Radushkevich, *Proc. Acad. Sci. U.S.S.R.,* **55,** 331 (1947).
19. F. K. Katsaros, PhD Dissertation (in prep.), University of Athens, 1997.
20. F. K. Katsaros, Th. A. Steriotis, A. K. Stubos, A. Ch. Mitropoulos, S. Tennison, N. Kanellopoulos, *Microporous Mat.,* in press.
21. R. M. Barrer, *Appl. Mat. Res.,* **2,** 29 (1963).
22. G. K. Papadopoulos, PhD Dissertation, University of Athens, 1993.
23. K. Beltsios and S. H. Carr, *J. Macrom. Sci., Phys. Ed.,* **B29,** 71 (1990).
24. M. Mulder, *Basic Principles of Membrane Technology,* Kluwer Academic Press, Dordrecht, 1991, Chap. 3.
25. A. Guinier and G. Fournet, *Small Angle X-ray Scattering,* Wiley, New York, 1955, Chap. 1.
26. J. D. Bernal, *Nature,* **183,** 141 (1959).
27. J. D. Bernal, *Nature,* **185,** 68 (1960).
28. J. D. Bernal, *Proc. Roy. Soc.,* **280A,** 299 (1964).
29. G. Mason, *J. Colloid Interf. Sci.,* **35,** 279 (1971).
30. N. Kanellopoulos, J. K. Petrou, and J. H. Petropoulos, *J. Colloid Interf. Sci.,* **96,** 90 (1983).
31. J. L. Finney and J. Wallace, *J. Non-Cryst. Sol.,* **43,** 165 (1981).
32. J. Millewski, *Ind. Eng. Chem. Prod. Res. Dev.,* **17,** 363 (1978).
33. J. L. Finney, *Proc. Roy. Soc.,* **319A,** 479 (1970).
34. H. J. Frost, *Amorphous Materials: Modelling of Structure and Properties,* V. Vitek, Ed., AIME, Pittsburgh, 1983, p. 33.
35. R. Williams, *The Geometrical Foundation of Natural Structure,* Dover Publications, New York, 1979.
36. A. B. Shelekhin, A. G. Dixon, and Y. H. Ma, *J. Membr. Sci.,* **83,** 181 (1993).
37. D. C. Bassett, *Comprehensive Polymer Science,* G. Allen and J. Bevington, Eds., Pergamon Press, Oxford, 1989.
    D. C. Bassett, *Polymer Characterization,* Vol. 2, C. Booth and C. Price, Eds., Pergamon Press, Oxford, 1989.
38. E. Baer, A. Hiltner, and H. D. Keith, *Science,* **235,** 1015 (1987).
39. J. V. Sanders and M. J. Murray, *Nature,* **275,** 201 (1978).
40. J. E. Markasky, *MRS Bull.,* **XIV,** 1 (1989).
41. F. Rousseaux and D. Tschoubar, *Carbon,* **15,** 63 (1977).